

Engineering a diamond spin-qubit with a nano-electro-mechanical system

Young-Ik Sohn,^{1,*} Srujan Meesala,^{1,*} Benjamin Pingault,^{2,*} Haig A. Atikian,¹
 Jeffrey Holzgrafe,^{1,2} Mustafa Gündoğan,² Camille Stavrakas,² Megan J. Stanley,²
 Alp Sipahigil,³ Joonhee Choi,^{1,3} Mian Zhang,¹ Jose L. Pacheco,⁴ John Abraham,⁴
 Edward Bielejec,⁴ Mikhail D. Lukin,³ Mete Atatüre,² and Marko Lončar¹

¹*John A. Paulson School of Engineering and Applied Sciences,
 Harvard University, 29 Oxford Street, Cambridge, MA 02138, USA*

²*Cavendish Laboratory, University of Cambridge,
 J. J. Thomson Avenue, Cambridge CB3 0HE, UK*

³*Department of Physics, Harvard University,
 17 Oxford Street, Cambridge, MA 02138, USA*

⁴*Sandia National Laboratories, Albuquerque, NM 87185, USA*

The realisation of a distributed quantum network requires long-lived memory qubits such as electron spins efficiently interfaced with indistinguishable optical photons. Due to dynamic fluctuations in the solid-state environment, it remains a challenge to identify a solid-state emitter that simultaneously offers excellent optical properties and long-lived qubit coherence. Specifically, the impact of thermal phonons is irreversible, and fundamentally limits qubit coherence. Here, we employ silicon-vacancy (SiV) colour centres in diamond, known for their excellent optical properties, and demonstrate an approach to improve their phonon-limited spin coherence. Using a diamond nano-electro-mechanical system (NEMS), we control the SiV electronic structure by tuning strain, allowing us to both probe and quench the interaction of the colour centre with phonons. This approach also provides a scalable platform to overcome optical inhomogeneity among emitters. The large wavelength tunability and improved spin coherence that we demonstrate make the SiV an attractive platform for the realisation of a quantum network.

Solid-state emitters offer the key advantage of scalability when used as building blocks for a quantum network. Nevertheless, there are outstanding challenges for linking multiple distant qubits at the single-emitter level. For instance, nitrogen-vacancy (NV) centres in diamond exhibit electronic spin-coherence times reaching a second [1], but naturally emit only a small fraction of their fluorescence as coherent (zero-phonon-line) photons. Efforts to address this challenge using

* These authors contributed equally

optical cavities [2–4] make the optical transition frequencies of the NV centre unstable due to its sensitivity to fluctuating electric fields in diamond nanostructures [5]. Recently, the silicon-vacancy (SiV) centre in diamond, exhibiting superior optical properties owing to its inversion symmetry [6], has been used to realise photon-mediated entanglement [7] and a bright fibre-coupled source of coherent photons [8]. Despite these advances, as a quantum memory, the SiV is limited by its short spin-coherence time due to spin-orbit-mediated interactions with thermal lattice phonons [9–13]. In this work, we control the static strain environment of the SiV, and increase the energy scale of the resonant phonon absorption process to far above the thermal energy ($k_B T \approx 0.3 \text{ meV} \approx h \times 80 \text{ GHz}$ at the experimental temperature, $T = 4 \text{ K}$). The resulting depletion of thermal phonons seen by the SiV leads to an improvement in its spin-coherence time.

The NEMS device used is a monolithic single-crystal diamond cantilever with metal electrodes patterned above and below it [14], as shown in the scanning electron microscope (SEM) image in Fig. 1a. An opening in the top electrode allows optical access to SiV centres inside the diamond cantilever. SiV centres are located in an array, (Fig. 1b) precisely positioned by focused ion-beam (FIB) implantation of $^{28}\text{Si}^+$ ions [15, 16]. Upon applying a DC voltage across the electrodes, the cantilever deflects downwards due to electrostatic attraction. This results in controllable static strain directed predominantly along the long axis of the cantilever, oriented along the [110] crystal axis. The strain profile can be visualized in the finite-element-method (FEM) simulation in Fig. 1c. While there are usually four equivalent orientations of the SiV in the diamond crystal, application of strain with our device generates two distinct classes as indicated by the blue and red arrows in Fig. 1c. In what follows, we mainly address transverse-orientation SiVs (labelled blue, and shown in detail in inset of Fig. 1c), which predominantly experience strain in the plane normal to their highest symmetry axis (E_g -strain [14]).

First, we demonstrate tuning of the electronic structure of the SiV centre using our NEMS device. The electronic structure of the negatively charged SiV centre (Fig. 2a) is characterised by a ground-state (GS) and excited-state (ES) separation of 407 THz, which corresponds to an optical wavelength of 737 nm [17]. The GS and ES each contain two distinct orbital branches whose degeneracy is partially lifted by spin-orbit coupling [18]: $|1\rangle, |2\rangle$ in the GS split by 46 GHz, and $|3\rangle, |4\rangle$ in the ES split by 255 GHz at zero strain. This results in four optical transitions A, B, C and D between the ground and excited manifolds. Photoluminescence excitation (PLE) spectra taken at 4 K reveal a separation of A and D transitions upon applying strain as shown in Fig. 2b. This result is in good quantitative agreement with a previous experiment on a dense ensemble of SiVs [19]. Further, for axially oriented SiVs (labelled red in Fig. 1c), we can tune the mean transition wavelength (frequency) by 0.3 nm (150 GHz) [14], which is approximately 10 times the

typical inhomogeneity in optical transitions [20]. A complete characterisation of the SiV strain Hamiltonian is presented in Ref. [14]. Since SiV centres are insensitive to electric fields to first order [6], our strain-tuning approach is the primary means to adjust the wavelength of individual centres in a scalable manner.

The variations in GS and ES splittings (Fig. 2b) show that E_g -strain mixes orbitals within the GS and ES. As a consequence, the SiV centre couples to E_g -phonons that are resonant with the GS and ES splittings [21]. Using our device, we can tune the resonant frequency of this phonon absorption process which limits the spin coherence time of the centre at $T = 4$ K. We can increase the GS splitting from 46 GHz to 1.2 THz in the best case, and typically up to 500 GHz, where the tuning range is determined by various factors, such as the breakdown voltage and the SiV location inside the cantilever [14].

Tuning of GS splitting allows us to probe the phonon density of states (DOS) by measuring the thermal relaxation rate between ground state orbital branches with the time-resolved pump-probe technique (Fig. 2c) [14]. Measurements are performed in the frequency range from $\Delta_{\text{gs}} = 46$ GHz to 110 GHz where the technique can be applied [14]. This relaxation rate is a sum of the rates of phonon absorption, γ_{up} , and emission, γ_{down} (shown in Fig. 2a), which can be individually extracted using the theory described in [14]. Over the range of Δ_{gs} measured, phonon processes in both directions are observed to accelerate with increasing GS splitting, since the number of acoustic modes resonant with the phonon transition, i.e. the phonon DOS increases as $\sim \Delta_{\text{gs}}^n$ (n is influenced by the geometry surrounding the SiV [14]). However, if the GS splitting is increased far above 120 GHz (at temperature $T = 4$ K) as plotted in Fig. 2d, the phonon absorption rate (γ_{up}) is theoretically expected to reverse its initial trend. In this regime, the polynomial increase in phonon DOS is outweighed by an exponential depletion of thermal phonon occupation ($\sim \exp(-h\Delta_{\text{gs}}/k_B T)$) [21], and γ_{up} is rapidly quenched.

Such a suppression of phonon absorption at high strain can be used to improve the spin properties of the SiV. In the presence of a magnetic field, the SiV electronic levels further split into spin sub-levels and provide an optically accessible spin-qubit as shown in Fig. 3a [9, 10, 22]. We use coherent population trapping (CPT) through resonant laser excitation of the optical transitions C1 and C2 to pump the SiV into a dark state, a coherent superposition of the spin sub-levels $|1 \downarrow\rangle, |1 \uparrow\rangle$. When the two-photon detuning is scanned, preparation of the dark state results in a fluorescence dip, whose width is determined by the spin-dephasing and the optical pumping rate. In Fig. 3b, as we increase the GS orbital splitting with our device, the CPT signal narrows down, and reveals the presence of two separate dips. Further measurements in Ref. [14] suggest that the presence of two dips is due to interaction of the SiV electron spin with a neighbouring spin such

as a ^{13}C nuclear spin. Fig. 3c shows the decreasing linewidths of the two dips with increasing GS splitting, indicating an improved spin coherence time. Beyond a GS splitting of ~ 400 GHz, the linewidths saturate at ~ 1 MHz. At the highest strain condition, we eliminate the contribution of power-broadening by measuring the power dependence of CPT (Fig. 3d), and reveal a spin coherence time $T_2^* = 0.25 \pm 0.02 \mu\text{s}$ (compared with $T_2^* = 40$ ns without strain engineering [9, 10]). Further, the spin lifetime T_1 (measured by a pump-probe experiment similar to that in Fig. 2c) is also prolonged by increasing GS splitting (Fig. 2e), but does not saturate, unlike T_2^* . This saturation of T_2^* is suggestive of a secondary dephasing source, such as magnetic-field noise from the ^{13}C nuclear spin-bath in diamond [23, 24], which becomes dominant as phonon-induced decoherence is suppressed.

In conclusion, the SiV-NEMS platform developed here allows us to eliminate the primary source of spin dephasing, and improve both the coherence and the lifetime of the spin qubit. We note that alternatives to our strain-tuning approach involve operation at mK temperatures with more complex cryogenic setups, or phononic bandgap engineering to forbid propagation of 46 GHz acoustic modes, where nanofabrication at length-scales smaller than half the acoustic wavelength (120 nm) is required. As a next step, coherent control [12] can be used to dynamically decouple the electron spin from slowly-varying environmental fields, and infer the native spin coherence time (T_2) as is routinely done for NV centres [25]. Moreover, these NEMS capabilities can be combined with diamond nanophotonics to add wavelength tunability to existing SiV-photon interfaces [7, 8]. Such devices can allow interactions between distant emitters, and thereby, the realisation of scalable photonic quantum networks. Another natural extension of our work is to use the large strain susceptibility of the SiV GS orbitals, and the spin-orbit coupling to engineer coherent coupling of SiV spins to well-defined mechanical modes. This can enable strain-mediated coherent control of the spin [26–29], as well as strong single-phonon coupling in optomechanical crystals [30]. In such devices, strong spin-phonon coupling can be used to implement phonon-mediated two-qubit gates [31], quantum non-linearities required to generate single phonons [32–34], and hybrid interfaces with other physical systems, such as superconducting qubits [35].

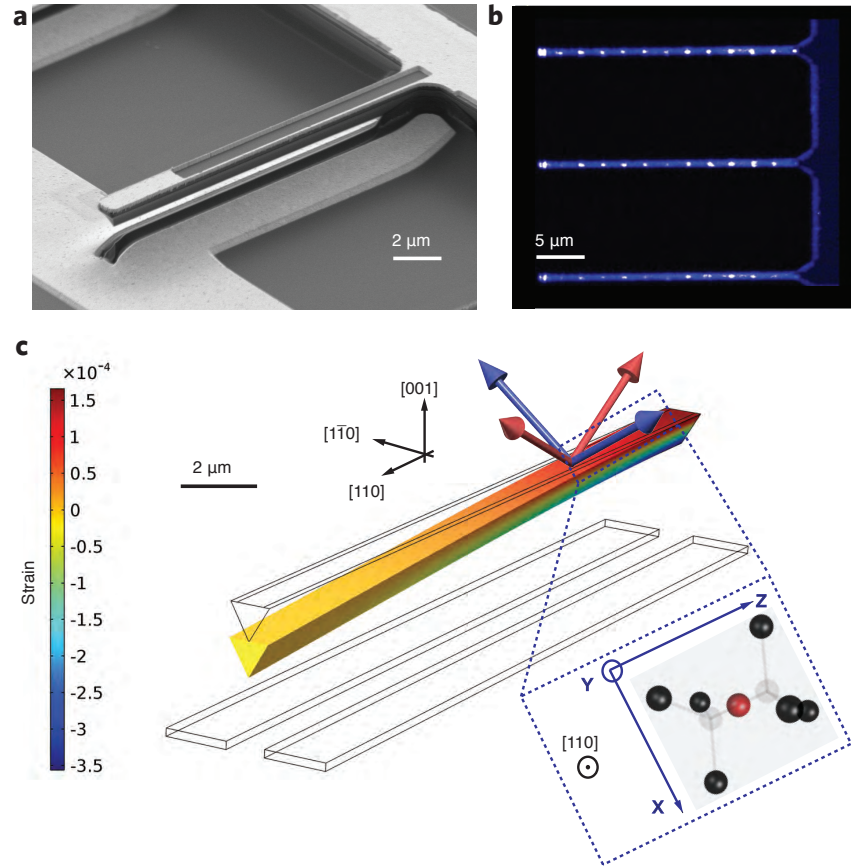


FIG. 1. (a) Scanning electron microscope (SEM) image of a representative diamond NEMS cantilever. Dark regions correspond to diamond, and light regions correspond to metal electrodes. (b) Confocal photoluminescence image of three adjacent cantilevers. The array of bright spots in each cantilever is due to fluorescence from SiV centres at these locations. (c) Finite-element-method (FEM) simulation of the displacement of the cantilever due to the application of a DC voltage of 200 V between the top and bottom electrodes. The component of the strain tensor along the long axis of the cantilever is calculated, and its magnitude is displayed using the colour scale. Crystal axes of diamond are indicated in relation to the geometry of the cantilever, whose long axis is oriented along the $[110]$ direction. Arrows on top of the cantilever indicate the highest symmetry axes of four possible SiV orientations, and their colour indicates separation into two distinct classes upon application of strain. SiVs shown by blue arrows are oriented along $[1\bar{1}1]$, $[\bar{1}11]$ directions, are orthogonal to the cantilever long-axis, and experience strain predominantly in the plane normal to their highest symmetry axis. SiVs shown by red arrows are oriented along $[111]$, $[\bar{1}\bar{1}1]$ directions, and experience appreciable strain along their highest symmetry axis. Inset shows the molecular structure of a blue-labelled SiV along with its internal axes, when viewed in the plane normal to the $[110]$ axis.

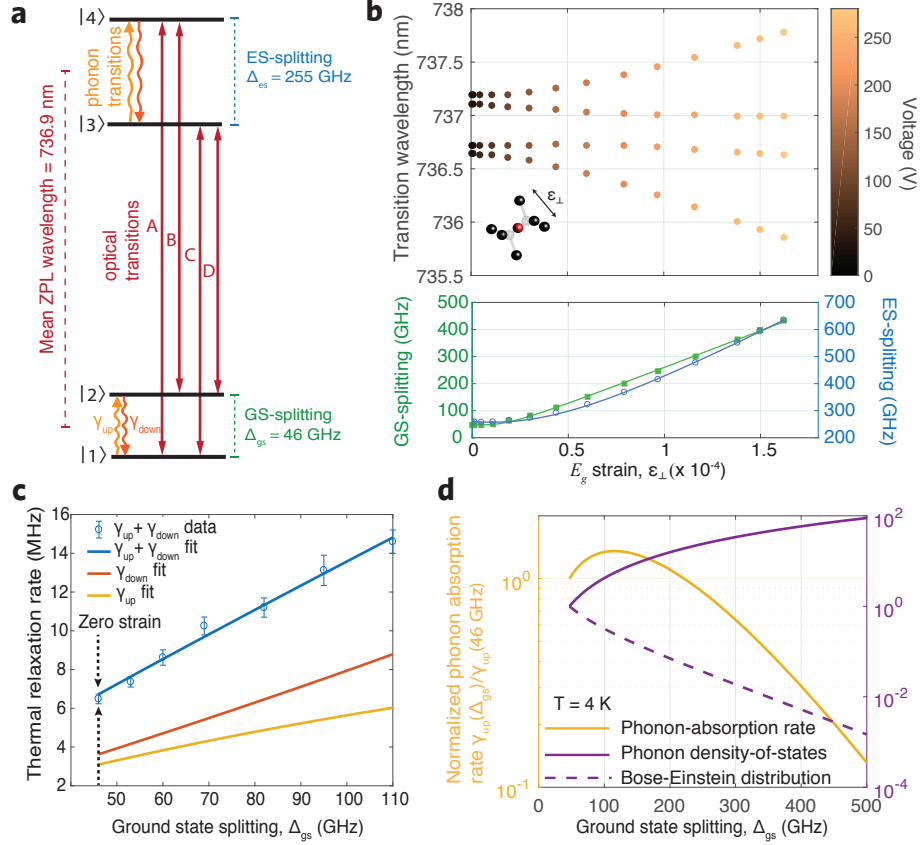


FIG. 2. (a) Electronic level structure of the SiV showing the mean zero phonon line (ZPL) wavelength, and frequency splittings between orbital branches in the ground state (GS) and excited state (ES) (Δ_{gs} and Δ_{es} respectively) at zero strain. The four optical transitions A, B, C, and D are depicted in the order of decreasing energy. Also shown are single-phonon transitions in the GS and ES manifolds. (b) Strain response of a blue-labelled SiV as shown in Fig. 1c. Wavelengths of the four optical transitions A, B, C, and D are recorded against strain (see [14] for raw PLE data with applied voltages, and strain-estimation procedure). The lower panel shows orbital splittings within GS (solid green squares) and ES (open blue circles) extracted from the optical transition wavelengths. Solid curves are fits to theory in [14]. (c) Thermal relaxation rates between GS orbital branches vs. their energy splitting. Fit to model in [14] allows extraction of the phonon-absorption rate γ_{up} and phonon-emission rate γ_{down} . (d) Theoretically calculated phonon-absorption rate $\gamma_{up}(\Delta_{gs})$ (solid yellow line) as a function of GS-orbital splitting Δ_{gs} at temperature $T = 4$ K. Left y -axis indicates the magnitude of this rate normalized to the value at zero strain, $\gamma_{up}(46$ GHz). Right y -axis indicates the two competing factors whose product determines the phonon-absorption rate: the phonon density-of-states (normalized to its value at zero strain), shown with the solid violet line, and the Bose-Einstein distribution, which determines the thermal occupation of acoustic modes, shown with the dashed violet line.

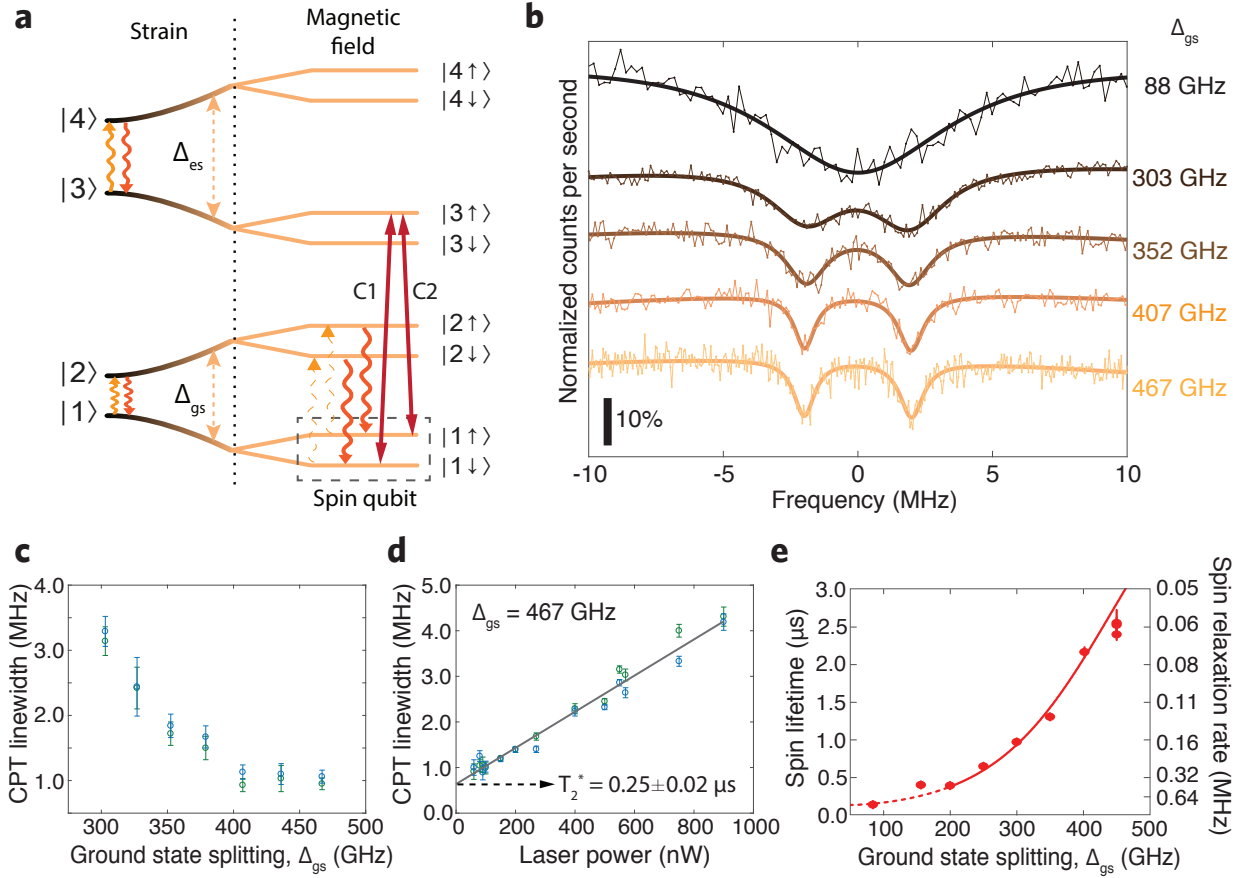


FIG. 3. (a) SiV level structure in the presence of strain and external magnetic field. A spin qubit is defined with levels $|1 \downarrow\rangle$ and $|1 \uparrow\rangle$ on the lower orbital branch of the GS. This qubit can be polarized, and prepared optically using the Λ -scheme provided by transitions C1 and C2. Phonon transitions within ground- and excited-state manifolds are also indicated. The upward phonon transition (phonon absorption process) can be suppressed at high strain, thereby mitigating the effect of phonons on the coherence of the spin qubit. (b) Coherent population trapping (CPT) spectra probing the spin transition at increasing values of the GS orbital splitting Δ_{gs} from top to bottom. Bold solid curves are Lorentzian fits. Optical power is adjusted in each measurement to minimize power-broadening. (c) Linewidth of CPT dips (estimated from Lorentzian fits) as a function of GS orbital splitting Δ_{gs} indicating improvement in spin coherence with increasing strain. (d) Power dependence of CPT-linewidth at the highest strain condition ($\Delta_{gs}=467$ GHz). Data points are estimated linewidths from CPT measurements, and the solid curve is a linear fit, which reveals an unbroadened linewidth of 0.64 ± 0.06 MHz corresponding to $T_2^* = 0.25 \pm 0.02 \mu\text{s}$. (e) Spin lifetime (T_1) as a function of GS orbital splitting Δ_{gs} . Data points are estimated from time-resolved pump-probe fluorescence measurements, solid curve is a fit to theory in [14].

-
- [1] Bar-Gill, N., Pham, L.M., Jarmola, A., Budker, D. & Walsworth, R. L. Solid-state electronic spin coherence time approaching one second. *Nat. Commun.* **4**, 1743 (2013).
- [2] Hausmann, B. J. M. et al. Coupling of NV centers to photonic crystal nanobeams in diamond. *Nano Letters* **13**, 5791-5796 (2013).
- [3] Faraon, A., Santori, C., Huang, Z., Acosta, V. M. & Beausoleil, R. G. Coupling of nitrogen-vacancy centers to photonic crystal cavities in monocrystalline diamond. *Phys. Rev. Lett.* **109**, 033604 (2012).
- [4] Riedel, D. et al. Deterministic enhancement of coherent photon generation from a nitrogen-vacancy centre in ultrapure diamond. *arXiv:1703.00815 [quant-ph]* (2017).
- [5] Chu, Y. & Lukin, M. D. Quantum optics with nitrogen-vacancy centers in diamond. *arXiv:1504.05990 [quant-ph]* (2015).
- [6] Sipahigil, A. et al. Indistinguishable photons from separated silicon-vacancy centers in diamond. *Phys. Rev. Lett.* **113**, 113602 (2014).
- [7] Sipahigil, A. et al. An integrated diamond nanophotonics platform for quantum-optical networks. *Science* **354**, 847-850 (2016).
- [8] Burek, M. J. et al. A fiber-coupled diamond quantum nanophotonic interface. *arXiv:1612.05285 [cond-mat.mes-hall]* (2016).
- [9] Pingault, B. et al. All-optical formation of coherent dark states of silicon-vacancy spins in diamond. *Phys. Rev. Lett.* **113**, 263601 (2014).
- [10] Rogers, L. J. et al. All-optical initialization, readout, and coherent preparation of single silicon-vacancy spins in diamond. *Phys. Rev. Lett.* **113**, 263602 (2014).
- [11] J. N. Becker, J. Görlitz, C. Arend, M. Markham & C. Becher. Ultrafast all-optical coherent control of single silicon vacancy colour centres in diamond. *Nat. Commun.* **7**, 13512 (2016).
- [12] Pingault, B. et al. Coherent control of the silicon-vacancy spin in diamond. *Nat. Commun.* **8**, 15579 (2017).
- [13] Orbach, R. Spin-lattice relaxation in rare-earth salts. *Proc. R. Soc. A* **A 264**, 458 (1961).
- [14] See supplementary information.
- [15] Tamura, S. et al. Array of bright silicon-vacancy centers in diamond fabricated by low-energy focused ion beam implantation. *Appl. Phys. Express* **7**, 11 (2014).
- [16] Schröder, T. et al. Scalable focused ion beam creation of nearly lifetime-limited single quantum emitters in diamond nanostructures. *arXiv:1610.09492 [quant-ph]* (2016).
- [17] Clark, C. D., Kanda, H., Kiflawi, I. & Sittas, G. Silicon defects in diamond. *Phys. Rev. B* **51**, 16681–16688 (1995).
- [18] Hepp, C., et al. Electronic structure of the silicon-vacancy center in diamond. *Phys. Rev. Lett.* **112**, 036405 (2014).
- [19] Sternschulte, H., Thonke, K., Sauer, R., Münzinger, P. C. & Michler, P. 1.681-eV luminescence center in chemical-vapor-deposited homoepitaxial diamond films. *Phys. Rev. B* **50**, 14554-14560 (1994).

- [20] Evans, R. E., Sipahigil, A., Sukachev, D. D., Zibrov, A. S. & Lukin, M. D. Narrow-linewidth homogeneous optical emitters in diamond nanostructures via silicon ion implantation. *Phys. Rev. Applied* **5**, 044010 (2016).
- [21] Jahnke, K. D. et al. Electron phonon processes of the silicon-vacancy centre in diamond. *New Journal of Physics* **17**, 043011 (2015).
- [22] Müller, T. et al. Optical signatures of silicon vacancy spins in diamond. *Nat. Commun.* **5**, 3328 (2014).
- [23] Togan, E., Chu, Y., Imamoglu, A. & Lukin, M. D. Laser cooling and real-time measurement of the nuclear spin environment of a solid-state qubit. *Nature* **478**, 497-501 (2011).
- [24] Balasubramanian, G. et al. Ultralong spin coherence time in isotopically engineered diamond. *Nature Materials* **8**, 383-387 (2009).
- [25] Childress, L. et al. Coherent dynamics of coupled electron and nuclear spin qubits in diamond. *Science* **314**, 281-285 (2006).
- [26] MacQuarrie, E. R., Gosavi, T. A., Jungwirth, N. R., Bhave, S. A. & Fuchs G. D. Mechanical spin control of nitrogen-vacancy centers in diamond. *Phys. Rev. Lett.* **111**, 227602 (2013).
- [27] Ouartchaiyapong, P., Lee, K. W., Myers, B. A. & Bleszynski-Jayich, A. C. Dynamic strain-mediated coupling of a single diamond spin to a mechanical resonator. *Nat. Commun.* **5**, 4429 (2014).
- [28] Teissier, J., Barfuss, A., Appel, P., Neu, E. & Maletinsky, P. Strain coupling of a nitrogen-vacancy center spin to a diamond mechanical oscillator. *Phys. Rev. Lett.* **113**, 020503 (2014).
- [29] Meesala, S. et al. Enhanced strain coupling of nitrogen-vacancy spins to nanoscale diamond cantilevers. *Phys. Rev. Appl.* **5**, 034010 (2016).
- [30] Burek, M. J. et al. Diamond optomechanical crystals. *Optica* **3**, 1404-1411 (2016).
- [31] Schuetz, M. J. A. et al. Universal quantum transducers based on surface acoustic waves. *Phys. Rev. X* **5**, 031031 (2015).
- [32] Ruskov, R. & Tahan, C. On-chip cavity quantum phonodynamics with an acceptor qubit in silicon. *Phys. Rev. B* **88**, 064308 (2013).
- [33] Söllner, I., Midolo, L. & Lodahl, P. Deterministic single-phonon source triggered by a single photon. *Phys. Rev. Lett.* **116**, 234301 (2016).
- [34] Cohen, J. D. et al. Phonon counting and intensity interferometry of a nanomechanical resonator. *Nature* **520**, 522 (2015).
- [35] Wallquist, M., Hammerer, K., Rabl, P., Lukin, M. & Zoller, P. Hybrid quantum devices and quantum engineering. *Physica Scripta* **T137**, 014001 (2009).

ACKNOWLEDGEMENTS

This work was supported by STC Center for Integrated Quantum Materials (NSF Grant No. DMR-1231319), ONR MURI on Quantum Optomechanics (Award No. N00014-15-1-2761), NSF EFRI ACQUIRE (Award No. 5710004174), the University of Cambridge, the ERC Consolidator

Grant PHOENICS, and the EPSRC Quantum Technology Hub NQIT (EP/M013243/1). B.P. thanks Wolfson College (University of Cambridge) for support through a research fellowship. Device fabrication was performed in part at the Center for Nanoscale Systems (CNS), a member of the National Nanotechnology Infrastructure Network (NNIN), which is supported by the National Science Foundation under NSF award no. ECS-0335765. CNS is part of Harvard University. Focused ion beam implantation was performed at the Laboratory Directed Research and Development Program and the Center for Integrated Nanotechnologies, an Office of Science (SC) user facility at Sandia National Laboratories operated for the DOE (contract DE-NA0003525) by National Technology and Engineering Solutions of Sandia, LLC., a wholly owned subsidiary of Honeywell International, Inc. We thank D. Perry for performing the focused ion beam implantation, and K. De Greve and M. W. Doherty for helpful discussions.